Modeling of Martensitic Transformations in Pure Iron by a Phase Field Approach Using Information from Atomistic Simulation

R. Schmitt, B. Wang, H. M. Urbassek, R. Müller

A phase field approach for martensitic transformations is introduced. The parameters are determined due to results from molecular dynamic simulations for pure iron. The continuum model is provided with the atomistic input data to examine the evolution of microstructure in 2D, both under the influence of external load and for interface motion through the transformation induced eigenstrain. Therefore, different configurations of the two phases are used. In addition, the energy evolution of the system is studied in detail during the transformation process. The numerical implementation of the model is performed with finite elements while an implicit time integration scheme is applied for the transient terms.

1 Introduction

Iron is an example for an allotropic material. In this paper two allotrops are of interest. At room temperature and ambient pressure α-iron is the stable phase. It has a body centered cubic (bcc) crystal structure. If the temperature is increased, it transforms into the γ-iron, also called austenite. The austenitic crystal lattice consists of face centered cubic (fcc) elementary cells. The change from austenite to α-iron depends on the cooling rate. If the probe is cooled slowly, the transformation is diffuse. For a sufficiently high cooling rate, a diffusionless transformation from the fcc to the bcc phase takes place, which is known as martensitic transformation in iron (Sandoval et al. (2009a)). The change of structure can be described by the Bain model (Bain (1924)) which defines a preexisting bcc unit cell within two fcc cells (Figure 2). To attain the martensitic bcc cell, a distortion of the preexisting bcc cell is necessary. The Bain model demonstrates that due to the crystallographic misfit an eigenstrain in the martensitic phase exits, which is considered in the proposed model for martensitic transformations.

The continuum mechanical background of phase transformations in solids is given by Fischer et al. (1994). Conventional models of phase transformations assume an infinitely sharp interface between the phases. Using this approach, energetic considerations yield the driving forces on the interfaces (Cherkaoui and Berveiller (2000)). However, tracking the interfaces can become difficult, so the numerical realization of this approach is cumbersome. The phase field concept can be applied as an alternative. In mathematical terms it is a regularization of a sharp interface approach: By the introduction of a scalar valued order parameter, which indicates the present phase, the discontinuities are regularized so that the transition zone is diffuse. Based on Chen et al. (1992) and Wang and Khachaturyan (1997) many phase field models on martensitic transformation have been developed, for example Artemev et al. (2000), Jin et al. (2001), which are based on the fast Fourier transformation (FFT) formalism. Kundin et al. (2011) propose an FFT-based approach, too, in which additionally dislocation kinetics are considered. Yamanaka et al. (2008) use a finite differences scheme to solve the field equations for an elastoplastic phase field model. Also Bartel et al. (2011) focus on the interaction of plasticity with martensitic phase transformations, which is based on the concept of energy relaxation. For considering complicated boundary conditions or complex material laws, the finite element method is more effective. In the context of phase field modeling of the martensitic transformation it is for example applied by Levitas et al. (2009), Hildebrand and Miehe (2011) or by Schmitt et al. (2013). Hildebrand and Miehe model two-variant martensitic laminates at large strains. The two martensitic variants are both stable states of the system. The thermomechanical model proposed by Levitas et al. (2009) considers stable and metastable phases of the martensitic transformation. However, the same elastic compliance tensor is used for both phases so that the different elastic properties of the phases cannot be taken into account.
Based on Schmitt et al. (2013), a finite element scheme is applied for the proposed phase field model for martensitic

transformations. The elasticity tensor depends linearly on the order parameter so that the different elastic properties of the different phases can be taken into account. Furthermore, the model considers stable and metastable phases. In this paper the parameters of the phase field model are chosen using the results from molecular dynamic (MD) simulation for pure iron. With a MD simulation, data from the atomistic scale can be gained, which is difficult to realize experimentally. On the other hand, length scales beyond 100 nm and time scales beyond a few ns are difficult to access in atomistic simulations. However, this is possible with the continuum phase field model provided with atomistic data.

The parameters are initially identified by a MD simulation for pure iron for the temperature $T = 100$ K. The temperature can be taken into account by the parameters in the separation potential which are provided by MD simulation. Then we verify the input data used for $T = 1300$ K.

Subsequently, we examine the evolution of the martensitic phase with the phase field model using the MD-parameters. In this context, we study the impact of an external load applied on the interface velocity. Additionally, the formation of the martensitic phase due to the transformation induced eigenstrain of a martensitic inclusion is considered. Since the model is based on a minimization of the global total energy, we also take the energy evolution during the martensitic transformation into account. Illustrative examples in 2D are studied. In these 2D problems a plane strain state is assumed.

2 Phase Field Model

In the phase field approach the present phase is indicated by an order parameter c_i, which is $c_i = 0$ for the austenitic phase and $c_i = 1$ for the ith martensitic orientation variant. The model is based on minimization of the global free energy $F = \int_V \psi \, \mathrm{d}V$. The local energy density or phase field potential ψ is split up into the elastic energy density W, the gradient energy densitiy ψ^{grad} and the separation potential ψ^{sep} (Schrade et al. (2007))

$$\psi(\varepsilon, c_i, \nabla c_i) = W(\varepsilon, c_i) + \psi^{\text{grad}}(\nabla c_i) + \psi^{\text{sep}}(c_i) \tag{1}$$

with

$$\psi^{\text{sep}} = \frac{G}{L} f(c_i), \qquad \psi^{\text{grad}} = \frac{1}{2} G\, L \, ||\nabla c_i||^2. \tag{2}$$

The gradient energy density ψ^{grad} yields a diffuse transition zone between the phases. The width of this zone is controlled by the constant parameter L. The parameter G is a measure for the characteristic interface energy density. Note that these parameters appear in both equations (2).

The function $f(c_i)$ in the separation potential ψ^{sep} in equation (2.1) is a Landau polynomial

$$f(c_i) = 1 + \frac{A}{2}\left(\sum_i c_i^2\right) - \frac{B}{3}\left(\sum_i c_i^3\right) + \frac{C}{4}\left(\sum_i c_i^2\right)^2 \tag{3}$$

On Figure 1, $f(c_i)$ is plotted for $i = 2$ martensitic orientation variants. It defines the stable and metastable states of the system: The local minimum of value 1 at $(0,0)$ corresponds to the metastable -at room temperature- austenitic phase, the two absolute minima of value 0 at $(1,0)$ and $(0,1)$ correspond to the first and the second martensitic orientation variant, respectively, which are the stable phases at room temperature. Thus, the energy landscape of the separation potential ensures that in each point only one phase occurs. The coefficients A, B and C in (3) configure the shape of $f(c_i)$ and therefore form the stable and metastable states of the system. These states of the system change with temperature, so A, B and C are temperature-dependent coefficients.

The elastic energy density

$$W(\varepsilon, c_i) = \frac{1}{2}[\varepsilon - \varepsilon^0(c_i)] : \mathbb{C}(c_i)[\varepsilon - \varepsilon^0(c_i)] \tag{4}$$

is a function of the linearized strain tensor ε. Furthermore, W considers the transformation-induced eigenstrain $\varepsilon^0(c_i)$ which arises due to the crystallographic misfit of the austenitic and the martensitic phases. The eigenstrain tensor $\varepsilon^0(c_i)$ and the elasticity tensor $\mathbb{C}$ depend linearly on the order parameters c_i

$$\varepsilon^0_{c_i}(c_i) = \sum_i c_i\, \varepsilon_i^0, \qquad \mathbb{C}(c_i) = \mathbb{C}_{\text{fcc}} + \sum_i c_i(\mathbb{C}_{\text{bcc}_i} - \mathbb{C}_{\text{fcc}}). \tag{5}$$

The eigenstrain ε_i^0 of the martensitic phase is calculated according to the Bain model (Bain (1924)) which defines a tetragonally distorted virtual bcc unit cell within two fcc unit cells (Figure 2). Taking the axes of the virtual bcc unit cell in Figure 2 as coordinate system, an extension in x- and y-direction and a compression in z-direction of the virtual bcc unit cell yield the martensitic crystal structure. For the 2D calulations we assume plane strain.
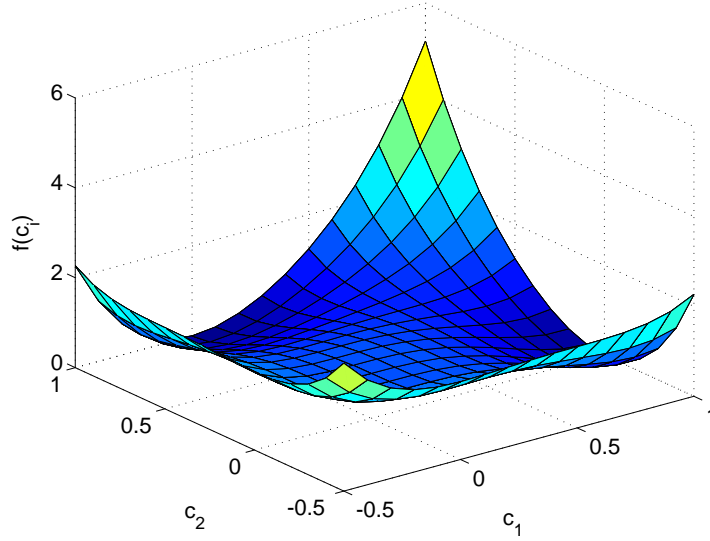
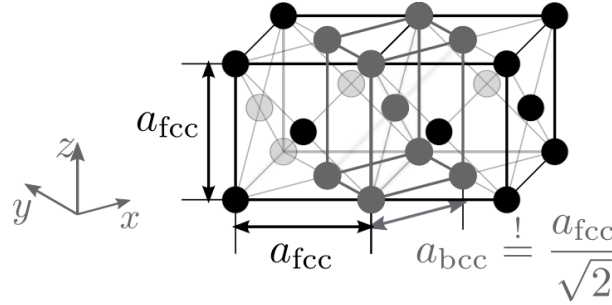Figure 1: Landau polynomial expansion $f(c_i) = f(c_1, c_2)$

Figure 2: Orientational relationship between the unit cells of the fcc and the bcc phase

Considering the geometrical relations of Figure 2 in the x-z-plane with $a_{\mathrm{bcc}} \overset{!}{=} \frac{a_{\mathrm{fcc}}}{\sqrt{2}}$ in x-direction and $a_{\mathrm{bcc}} \overset{!}{=} a_{\mathrm{fcc}}$ in z-direction results in the following eigenstrain tensor

$$\varepsilon_1^0 = \begin{bmatrix} \dfrac{a_{\mathrm{bcc}} - \dfrac{a_{\mathrm{fcc}}}{\sqrt{2}}}{\dfrac{a_{\mathrm{fcc}}}{\sqrt{2}}} & 0 \\ 0 & \dfrac{a_{\mathrm{bcc}} - a_{\mathrm{fcc}}}{a_{\mathrm{fcc}}} \end{bmatrix}. \tag{6}$$

A rotation of the coordinate system in Figure 2 about 90° results in an eigenstrain tensor with the same entries, however interchanged. In that way different martensitic orientation variants arise which need to be respected with different eigenstrain tensors ε_i^0.

To describe the formation of the microstructure, the order parameter is governed by a time-dependent Ginzburg-Landau equation (TDGL), i.e. the temporal evolution of each order parameters $\dot{c}_i$ is given by the variational derivative of the phase field potential ψ with respect to the order parameter c_i

$$\dot{c}_i = -M \frac{\delta \psi}{\delta c_i} = -M \left[\frac{\partial W}{\partial c_i} + G \left(\frac{1}{L} \frac{\partial f}{\partial c_i} - L \Delta c_i \right) \right]. \tag{7}$$

The mobility factor M is proportional to $\dot{c}_i$, thus it determines the kinetics of the microstructure evolution. The second field equation, which the mechanical quantities have to satisfy is the balance of linear momentum. For the paper at hand, inertia effects are neglected and the absence of volume forces is assumed, which yields the equilibrium condition

$$\mathrm{div}\boldsymbol{\sigma} = \mathbf{0}. \tag{8}$$

In (8), $\boldsymbol{\sigma}$ is the Cauchy stress tensor for which the constitutive relation

$$\boldsymbol{\sigma} = \frac{\partial \psi}{\partial \boldsymbol{\varepsilon}} = \mathbb{C}(c_i)\left(\boldsymbol{\varepsilon} - \boldsymbol{\varepsilon}^0(c_i)\right) \tag{9}$$

holds.

Equations (7) and (8) represent a non-linear time-dependent system of equations, coupled through the dependencies on the order parameter c_i. This problem is solved by applying a finite element scheme.

3 Numerical Implementation

The phase field model is implemented into a finite element framework with the mechanical displacements $\boldsymbol{u}$ and the order parameter c_i as nodal degrees of freedom, where i is the number of martensitic orientation variants considered. Thus, for a 2D implementation the number of degrees of freedom is $i + 2$. With the test functions $\boldsymbol{\eta}_u$ and η_{c_i} the weak forms of the field equations (7) and (8) is

$$\int_V \boldsymbol{\nabla}\boldsymbol{\eta}_u : \boldsymbol{\sigma} \, \mathrm{d}V = \int_{\partial V_t} \boldsymbol{\eta}_u \boldsymbol{t}^* \, \mathrm{d}A. \tag{10}$$

and

$$\int_V \eta_{c_i} \frac{\dot{c}_i}{M} \, \mathrm{d}V - \int_V \boldsymbol{\nabla}\eta_{c_i} \, \boldsymbol{q}_i \, \mathrm{d}V + \int_V \eta_{c_i} \left(\frac{\partial W}{\partial c_i} + \frac{G}{L}\frac{\partial f}{\partial c_i}\right) \mathrm{d}V = -\int_{\partial V} \eta_{c_i} \, q_i^* \, \mathrm{d}A, \tag{11}$$

where $\boldsymbol{q}_i = -G\,L\,\nabla c_i$. The necessary boundary conditions are given by $\boldsymbol{t}^* = \boldsymbol{\sigma} n$ for the stresses $\boldsymbol{\sigma}$ and by $q_i^* = \boldsymbol{q}_i \cdot \boldsymbol{n} = 0$ for $\boldsymbol{q}_i$ where $\boldsymbol{n}$ is the outer normal vector to the volume V.

For the 2D-plane strain problem of $\boldsymbol{u}$, $\boldsymbol{\varepsilon}$ and c_i, ∇c_i are discretized with shape functions N_I for node I, where the use of Voigt notation is denoted by an underbar $(\underline{\cdot})$ and nodal quantities by the superimposed hat $(\hat{\cdot})$

$$\underline{\boldsymbol{u}} = \sum_{I=1}^N N_I \, \hat{\underline{\boldsymbol{u}}}_I, \qquad\qquad \underline{\boldsymbol{\varepsilon}} = \sum_{I=1}^N \underline{\boldsymbol{B}}_I^u \, \hat{\underline{\boldsymbol{u}}}_I, \tag{12}$$

$$c_i = \sum_{I=1}^N N_I \, \hat{c}_{i_I}, \qquad\qquad \underline{\nabla c}_i = \sum_{I=1}^N \underline{\boldsymbol{B}}_I^{c_i} \, \hat{c}_{i_I} \tag{13}$$

$$\dot{c}_i = \sum_{I=1}^N N_I \, \hat{\dot{c}}_{i_I} \tag{14}$$

with

$$\underline{\boldsymbol{B}}_I^u = \begin{bmatrix} N_{I,x} & 0 \\ 0 & N_{I,y} \\ N_{I,y} & N_{I,x} \end{bmatrix} \qquad \text{and} \qquad \underline{\boldsymbol{B}}_I^{c_i} = \begin{bmatrix} N_{I,x} \\ N_{I,y} \end{bmatrix}. \tag{15}$$

These discretizations applied to the left hand sides of equations (10), (11) yield the nodal residuals as a function of the nodal degrees of freedom $\hat{\underline{d}}_J = (\hat{\underline{u}}_J, c_{i_J})^T$ and the rates $\hat{\dot{\underline{d}}}_J$,

$$\underline{\boldsymbol{R}}_I(\hat{\underline{d}}_J, \hat{\dot{\underline{d}}}_J) = \begin{bmatrix} \boldsymbol{R}_I^u(\hat{\underline{d}}_J, \hat{\dot{\underline{d}}}_J) \\ R_I^{c_1}(\hat{\underline{d}}_J, \hat{\dot{\underline{d}}}_J) \\ \vdots \\ R_I^{c_i}(\hat{\underline{d}}_J, \hat{\dot{\underline{d}}}_J) \end{bmatrix} = \begin{bmatrix} \int_V (\underline{\boldsymbol{B}}_I^u)^T \, \underline{\boldsymbol{\sigma}} \, \mathrm{d}V \\ \int_V N_I \frac{\dot{c}_1}{M} \, \mathrm{d}V - \int_V \underline{\boldsymbol{B}}_I^{c_1 \, T} \boldsymbol{q}_1 \, \mathrm{d}V + \int_V N_I \left(\frac{\partial W}{\partial c_1} + \frac{G}{L}\frac{\partial f}{\partial c_i}\right) \mathrm{d}V \\ \vdots \\ \int_V N_I \frac{\dot{c}_i}{M} \, \mathrm{d}V - \int_V \underline{\boldsymbol{B}}_I^{c_i \, T} \boldsymbol{q}_i \, \mathrm{d}V + \int_V N_I \left(\frac{\partial W}{\partial c_i} + \frac{G}{L}\frac{\partial f}{\partial c_i}\right) \mathrm{d}V \end{bmatrix}. \tag{16}$$

For the transient terms the Euler backward method is applied. The stiffness matrix is

$$\underline{\boldsymbol{K}}_{IJ} = \frac{\partial \underline{\boldsymbol{R}}_I}{\partial \hat{\underline{d}}_J} = \begin{bmatrix} \boldsymbol{K}_{IJ}^{uu} & \boldsymbol{K}_{IJ}^{uc_i} \\ \boldsymbol{K}_{IJ}^{c_i u} & \boldsymbol{K}_{IJ}^{c_i c_j} \end{bmatrix}, \tag{17}$$

with the submatrices

$$\underline{\boldsymbol{K}}_{IJ}^{uu} = \underline{\boldsymbol{k}}_{IJ}^{uu} \qquad\qquad (2 \times 2) \qquad\qquad (18)$$

$$\underline{\boldsymbol{K}}_{IJ}^{uc_i} = [\underline{\boldsymbol{k}}_{IJ}^{uc_1}, ..., \underline{\boldsymbol{k}}_{IJ}^{uc_i}] \qquad\qquad (1 \times i) \qquad\qquad (19)$$

$$\underline{\boldsymbol{K}}_{IJ}^{c_i u} = \left[\begin{array}{c} \underline{\boldsymbol{k}}_{IJ}^{c_1 u} \\ \vdots \\ \underline{\boldsymbol{k}}_{IJ}^{c_i u} \end{array} \right] \qquad\qquad (i \times 1) \qquad\qquad (20)$$

$$\underline{\boldsymbol{K}}_{IJ}^{c_i c_j} = \left[\begin{array}{ccc} \underline{\boldsymbol{k}}_{IJ}^{c_1 c_1} & ... & \underline{\boldsymbol{k}}_{IJ}^{c_1 c_i} \\ ... & ... & ... \\ \underline{\boldsymbol{k}}_{IJ}^{c_j c_1} & ... & \underline{\boldsymbol{k}}_{IJ}^{c_j c_j} \end{array} \right] \qquad\qquad (i \times j) \qquad\qquad (21)$$

$$\text{with } j = (1, ..., i). \qquad\qquad (22)$$

The matrix entries can be calculated with $\tilde{\underline{\boldsymbol{\sigma}}} = (\mathbb{C}_{\text{bcc}} - \mathbb{C}_{\text{fcc}}) \left(\underline{\boldsymbol{\varepsilon}} - \underline{\boldsymbol{\varepsilon}}^0(c_i) \right)$ and $\underline{\boldsymbol{\sigma}}_i^0 = \underline{\mathbb{C}}(c_i)\underline{\boldsymbol{\varepsilon}}_i^0$ as follows

$$\underline{\boldsymbol{k}}_{IJ}^{uu} = \int_V (\underline{\boldsymbol{B}}_I^u)^T \, \underline{\mathbb{C}}(c_i \, \underline{\boldsymbol{B}}_J^u \, \mathrm{d}V$$

$$\underline{\boldsymbol{k}}_{IJ}^{uc_i} = \underline{\boldsymbol{k}}_{IJ}^{c_i u} = \int_V (\underline{\boldsymbol{B}}_I^u)^T \left(\tilde{\underline{\boldsymbol{\sigma}}} - \underline{\boldsymbol{\sigma}}_i^0 \right) N_J \, \mathrm{d}V$$

$$\underline{\boldsymbol{k}}_{IJ}^{c_i c_i} = \underline{\boldsymbol{k}}_{IJ}^{c_j c_j} = \int_V G \, L \, (\underline{\boldsymbol{B}}_I^{c_i})^T \, \underline{\boldsymbol{B}}_J^{c_i} + N_I \left(\left(\underline{\boldsymbol{\varepsilon}}_i^0 \right)^T \left(\underline{\boldsymbol{\sigma}}_i^0 - 2\tilde{\underline{\boldsymbol{\sigma}}} \right) + \frac{G}{L} \frac{\partial^2 f}{\partial c_i^2} \right) N_J \, \mathrm{d}V$$

$$\underline{\boldsymbol{k}}_{IJ}^{c_i c_j} = \int_V N_I \left(-\tilde{\underline{\boldsymbol{\sigma}}} \left(\underline{\boldsymbol{\varepsilon}}_i^0 + \underline{\boldsymbol{\varepsilon}}_j^0 \right) + \underline{\boldsymbol{\varepsilon}}_j^0 \, \underline{\boldsymbol{\sigma}}_i^0 + \frac{G}{L} \frac{\partial^2 f}{\partial c_i c_j} \right) N_J \, \mathrm{d}V \quad (i \neq j)$$

$$\underline{\boldsymbol{k}}_{IJ}^{c_j c_i} = \int_V N_I \left(-\tilde{\underline{\boldsymbol{\sigma}}} \left(\underline{\boldsymbol{\varepsilon}}_i^0 + \underline{\boldsymbol{\varepsilon}}_j^0 \right) + \underline{\boldsymbol{\varepsilon}}_i^0 \, \underline{\boldsymbol{\sigma}}_j^0 + \frac{G}{L} \frac{\partial^2 f}{\partial c_i c_j} \right) N_J \, \mathrm{d}V \quad (i \neq j).$$

The damping matrix is given by

$$\underline{\boldsymbol{D}}_{IJ} = \frac{\partial \underline{R}_I}{\partial \hat{\underline{d}}_J} = \int_V \left[\begin{array}{ccc} 0 & 0 & 0 \\ 0 & 0 & 0 \\ 0 & 0 & \underline{\boldsymbol{D}}_{IJ}^{c_i c_j} \end{array} \right] \mathrm{d}V \qquad\qquad (23)$$

with

$$\underline{\boldsymbol{D}}_{IJ}^{c_i c_j} = \left[\begin{array}{cccc} \frac{1}{M} N_I^2 & 0 & ... & 0 \\ 0 & \ddots & 0 & \vdots \\ \vdots & 0 & \ddots & 0 \\ 0 & ... & 0 & \frac{1}{M} N_I^2 \end{array} \right] \qquad\qquad (i \times j) \qquad\qquad (24)$$

$$\text{with } j = (1, ..., i). \qquad\qquad (25)$$

For the evaluation of the integrals Gauß quadrature is used. The equations are implemented into a finite element scheme using a four node quadrilateral plane element with bilinear shape functions.

4 Parameters in Cooperation with MD-simulation

In this section the model parameters are chosen, based on MD simulation of pure iron. The MD parameters used are determined as follows.

4.1 Atomistic Simulation Method

Atomistic simulation may be employed to study the energetics and dynamics of solid-state phase transitions; a recent review is available which summarizes the state of the art for the iron system: Urbassek and Sandoval (2012). For such studies, the interatomic interaction potentials have to be chosen with care. Engin et al. (2008)

analyzed available potentials for iron and concluded that there are only few potentials which implement the α-γ transition. Among these, in the class of embedded-atom method (EAM) potentials (Daw et al. (1993)), the Meyer-Entel potential (Meyer and Entel (1998)) is able to describe the phase transition in Fe. It has several advantages: The free enthalpies of the bcc- and the fcc-phase cross at a transition temperature predicting the bcc phase to be stable above this temperature and the fcc phase to be stable below this temperature. Due to its simple EAM form, the Meyer-Entel potential can be calculated sufficiently fast. This potential has been used successfully in the past to study the phase transition in Fe. Bulk iron (Entel et al. (1998, 2000); Sandoval et al. (2009b)) was investigated as well as Fe nanoclusters (Entel et al. (2004)) nanowires (Sandoval and Urbassek (2009a,b,c)), and supported thin films (Kadau et al. (1999); Kadau and Entel (1999)). Finally, the dynamics of the Nishiyama-Wassermann transformation was analyzed in detail for this potential (Sandoval and Urbassek (2009c); Sandoval et al. (2009a)). We use classical (fully 3D) molecular-dynamics simulations to determine the properties of the bcc and the fcc phase as well as that of a bcc/fcc interface. Details of the approach have been given in Wang and Urbassek (2013). All calculations are performed with the open-source LAMMPS code (Sandia (1997-2012)). The lattice constants of the pure phases are determined as follows. A crystallite is relaxed with periodic boundary conditions; here, the pressure P is controlled to be zero by allowing the volume to change, while the temperature is set to the desired temperature T by a thermostat. After the equilibration, the simulation runs for 50 ps under these conditions. We take the average of the lattice constant during these 50 ps as the estimate of the lattice constant at this temperature. The elastic constants are also determined in these systems. After equilibration at zero pressure, we put well-defined strains to the system by changing the length of the simulation box. By measuring the resulting stress components, the elastic constants can be determined. Again, a temporal average allows us to get rid of temperature-induced fluctuations. The calculation of the free-energy difference between the bcc and fcc phase requires more effort. As described in detail in Engin et al. (2008), we implemented two schemes in order to allow for a reliable calculation: the method of metric scaling as introduced in Miller and Reinhardt (2000) and the method of thermodynamic integration (Mei and Davenport (1992); Frenkel and Smit (2002)). Both methods give results in good agreement with each other. The calculation of the interface energy and velocity needs a biphasic crystal. We construct an interface between a bcc crystal and a fcc crystal according to the Nishiyama-Wassermann orientation relationship (Nishiyama (1934); Wassermann (1933)) as detailed in Sandoval et al. (2009a). Using periodic boundary conditions at all boundaries of the system, we can calculate the specific phase boundary energy E by

$$E = \frac{E_{\text{total}} - (E_{\text{bcc}} N_{\text{bcc}} + E_{\text{fcc}} N_{\text{fcc}})}{2A}, \tag{26}$$

where E_{total} is the total potential energy of the simulation volume, A is the interface area, N_{bcc} is the number of atoms, and E_{bcc} the cohesive energy on the bcc side; analogously for the fcc side. The factor of 2 in the denominator takes into account that due to the periodic boundary conditions, there are effectively two interfaces in the system. Note that this interface is under zero stress. For the determination of the interface velocity, we let the system evolve freely (at constant temperature and pressure). The interface then spontaneously starts moving in the direction normal to the interface such that the phase with the higher free energy shrinks. We average the speed of the interface over time and thus determine the interface velocity.

4.2 Determination of the Parameters for the Phase Field Model

Based on the results of the atomistic simulations the parameters for the phase field model are chosen. Therefore a single martensitic orientation variant ($i = 1$) is considered, so that in the following for the order parameter c is used instead of c_1. With the atomic volumes given by MD for fcc and bcc for the temperatures $T = 100$ K and $T = 1300$ K, the lattice constants are calculated easily due to the cubic crystal structures of both phases. With the lattice constants, the eigenstrain tensors ε_1^0 for both temperatures are determined according to (6) with

$$\varepsilon_1^0(T = 100\,\text{K}) = \begin{bmatrix} -0.2217 & 0.0 \\ 0.0 & 0.1007 \end{bmatrix} \tag{27}$$

$$\varepsilon_1^0(T = 1300\,\text{K}) = \begin{bmatrix} -0.2063 & 0.0 \\ 0.0 & 0.1091 \end{bmatrix}. \tag{28}$$

Using the elastic constants of the fcc- and bcc-lattices resulting from MD simulations, effective Lamé parameters are calculated in agreement with Pimpinelli and Villain (1998)

$$\overline{\lambda} = \frac{1}{5}(C_{11} + 4C_{12} - 2C_{44}), \qquad \overline{\mu} = \frac{1}{5}(C_{11} - C_{12} + 3C_{44}) \tag{29}$$

which eventually yield the effective isotropic elasticity tensors for the austenitic and the martensitic phase, respectively

$$\overline{\mathbb{C}}^{\text{fcc}} = \begin{bmatrix} 221\,880 & 149\,840 & 0 \\ 149\,840 & 221\,880 & 0 \\ 0 & 0 & 36\,030 \end{bmatrix} \frac{\text{N}}{\text{mm}^2}, \qquad \overline{\mathbb{C}}^{\text{bcc}} = \begin{bmatrix} 292\,700 & 106\,250 & 0 \\ 106\,250 & 292\,700 & 0 \\ 0 & 0 & 93\,220 \end{bmatrix} \frac{\text{N}}{\text{mm}^2}. \qquad (30)$$

The characteristic interface energy density is calculated atomistically according (26) (cf. Wang and Urbassek (2013)): $G = 0.96 \frac{\text{J}}{\text{m}^2}$. This value is comparable to the energy densities used for other phase field models, e. g. in Schrade et al. (2008). The transition zone $L = 10$ nm is sufficiently small to resolve several finite elements.

The remaining parameters are the coefficients A, B and C of the Landau polynomial (3) and the mobility parameter M of the TDGL (7). To determine the coefficients A, B and C, the energy per atom is calculated for the states the atom occupies during the martensitic transformation with MD simulation. These data are plotted in Figure 3(a),
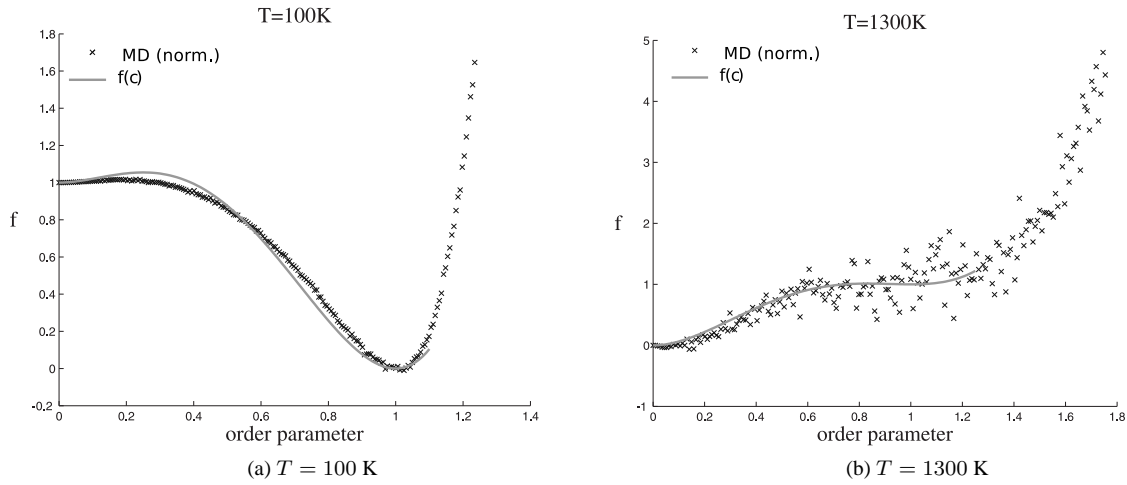

(a) $T = 100$ K

(b) $T = 1300$ K

Figure 3: Energy barrier resulting from MD (black curve), Landau polynomial $f(c)$ (grey curve)

(black curve) for the temperature $T = 100$ K, with the order parameter c on the x-axis. The curve is normalized, so that the ordinate-value $f = 1$ for the local minimum. Thus, the black curve resulting from MD-simulations corresponds to the Landau polynomial (3). To determine the coefficients A, B and C, we apply a least-square methode (grey curve in Figure 3(a)) and attain $A = 6$, $B = 30$ and $C = 24$ while $B = 3A + 12$ and $C = 2A + 12$ must be satisfied (Yamanaka et al. (2008)). These relations between the coefficients ensure the local minimum at $c = 0$ and the global minimum at $c = 1$. For $T = 100$ K those extrema correspond to the metastable phase austenite and the stable phase martensite, respectively.

Using these parameters a beam with a length of 176.5 nm is simulated to determine the mobility parameter M.

The initial configuration can be seen in Figure 4(a): The left half of the beam is austenitic, depicted in black, the right half martensitic, depicted in white; no external load is applied. Figure 3(a) indicates, that for $T = 100$ K, austenite is the metastable phase and martensite the energetically more favourable stable phase. Concerning the energy of the initial configuration depicted in Figure 4(a), the martensitic phase has an eigenstrain ε^0 which increases the elastic energy of the system while the austenitic phase has a contribution resulting from the separation potential ψ^{sep}. Additionally, the interface between the phases contributes to the gradient energy density ψ^{grad}. Hence, the system minimizes the global total energy by shifting the interface between the phases to the left (Figure 4(c)) until the beam is completely martensitic (Figure 4(e)). For a purely martensitic material, there is no contribution for the gradient energy densitiy ψ^{grad} since there is no interface. Furthermore, the energy contribution of the separation potential ψ^{sep} is zero because all points of the system are in the global minimum at $c = 1$.

The mobility parameter M in (7) is directly proportional to the time derivative of the order parameter $\dot{c}$, so that M determines the velocity of the evolution of the microstructure. During the transformation process, the x-coordinate of the interface is tracked so that the interface velocity can be detected. In the next step, the mobility parameter M is adapted until the interface velocity v_{if} of the simulation is in accordance with the interface velocity given by MD simulation $v_{\text{if}}^{MD} = 24.2 \frac{\text{m}}{\text{s}}$. This is the case for $\mathbf{M = 9.6 \cdot 10^6 \frac{\text{mm}^2}{\text{N s}}}$ which leads to the interface velocity $\mathbf{v_{\text{if}} = 24.11 \frac{\text{m}}{\text{s}}}$.

This procedure is repeated for a temperature $T = 1300$ K. The energy per atom during the martensitic transformation can be seen in Figure 3(b) (black curve). It indicates, that for $T = 1300$ K austenite is the stable and

(a) $t = 0\,\mathrm{ns}$

(b) $t = 0\,\mathrm{ns}$

(c) $t = 1.26\,\mathrm{ns}$

(d) $t = 1.26\,\mathrm{ns}$

(e) $\mathbf{t = 3.8\,ns}$

(f) $\mathbf{t = 3.2\,ns}$

Figure 4: interface motion for a two-phase beam, black: austenite, white: martensite
(a),(c),(e): $T = 100$ K, (b),(d),(f): $T = 1300$ K

martensite the metastable phase. Thus, the Landau polynomial has a global minimum is at $c = 0$ and the local minimum at $c = 1$, so it becomes for i martensitic orientation variants

$$ f(c_i) = \frac{A}{2}\left(\sum_i c_i^2\right) - \frac{B}{3}\left(\sum_i c_i^3\right) + \frac{C}{4}\left(\sum_i c_i^2\right)^2. \tag{31}$$

For the grey curve in Figure 3(b), which results again from the least square method, this is ensured by the relations $B = 3A - 12$ and $C = 21 - 12$ for the coefficients in (31), which yields $A = 15$, $B = 33$ and $C = 18$. Using these coefficients, the initial configuration shown in Fig 4(b) is employed: a beam with no external loads applied, on the right side martensitic (depicted in white) and on the left austenitic (depicted in black). For this calculation, the same mobility parameter $\mathbf{M} = \mathbf{9.6 \cdot 10^6}\ \frac{\mathbf{mm^2}}{\mathbf{N\,s}}$ than for $T = 100$ K is considered. The resulting interface velocity for $T = 1300$ K is $\mathbf{v}_{\mathrm{if}} = \mathbf{28.52}\ \frac{\mathrm{m}}{\mathrm{s}}$. This value fits the velocity from MD simulation $v_{\mathrm{if}}^{MD} = 26.0\ \frac{\mathrm{m}}{\mathrm{s}}$ quite good. We interpreted this as verification of the mobility constant M. As a result, for this simulation the mobility constant M hardly depends on the temperature T.

5   Numerical Simulation

For the following numerical simulations, the parameters derived in Section 4 for the temperature $T = 100$ K are used. We consider a single martensitic orientation variant ($i = 1$), so that the formation of a single phase can be studied individually. A further martensitic orientation variant can be incorporated readily.

5.1   External Loads on a Two-phase Beam

In the first example the dependence of the interface velocity v_{if} on an extenal load is studied. Therefore, again the beam with the initial configuration of Section 4 is applied (Figure 4(a)/(b)) with martensite on the right side of the beam (depicted in white) and austenite on the left (depicted in black). The material parameters derived in section 4 for $T = 100$ K are considered, thus, for the eigenstrain ε^0 (6) is taken into account. It corresponds to pressure in horizontal direction and tension in vertical direction.

With this study, we noticed a correlation between the external load applied, the eigenstrain ε^0 and the interface velocity v_{if}. When the eigenstrain ε^0 is supported by applying pressure $\sigma^{\mathrm{a}} = -\mathbf{22.7}\ \frac{\mathrm{N}}{\mathrm{mm^2}}$ in horizontal direction of the beam, the interface velocity $\mathbf{v}_{\mathrm{if}} = \mathbf{26.12}\ \frac{\mathrm{m}}{\mathrm{s}}$ (Figure 5(a)) is higher than with no load applied (see above $\mathbf{v}_{\mathrm{if}} = \mathbf{24.11}\ \frac{\mathrm{m}}{\mathrm{s}}$). In analogy, applying tension $\sigma^{\mathrm{a}} = \mathbf{22.7}\ \frac{\mathrm{N}}{\mathrm{mm^2}}$ in horizontal direction, which works against the eigenstrain ε^0, leads to a lower velocity $\mathbf{v}_{\mathrm{if}} = \mathbf{22.35}\ \frac{\mathrm{m}}{\mathrm{s}}$ (Figure 5(c)). So, the interface velocity v_{if} is affected by external loads, depending on the eigenstrain ε^0.
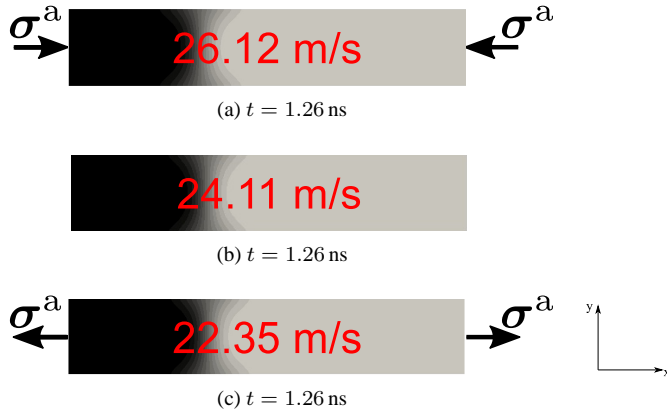
(a) $t = 1.26\,\text{ns}$

(b) $t = 1.26\,\text{ns}$

(c) $t = 1.26\,\text{ns}$

Figure 5: Interface motion for a two-phase beam under external load, black: austenite, white: martensite

(a) $t = 0\,\text{ns}$ (b) $\mathbf{t = 0.04\,ns}$ (c) $\mathbf{t = 0.1\,ns}$ (d) $\mathbf{t = 0.4\,ns}$ (e) $\mathbf{t = 1.5\,ns}$ (f) $\mathbf{t = 5.5\,ns}$
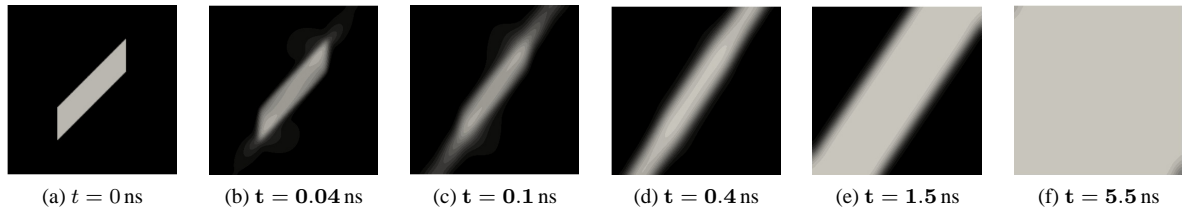
Figure 6: Evolution of the martensitic phase for a martensitic inclusion (white)

5.2 Martensitic Inclusion in an Austenitic Matrix

With the following example the martensitic evolution is studied for a martensitic inclusion in an austenitic matrix with an edge length of 176.5 nm. The initial configuration can be seen in Figure 6(a), where the austenitic matrix ($c = 0$) and the martensitic inclusion ($c = 0.9$) are depicted in black and white, respectively. No external loads are applied so that the boundaries are stress free.

Regarding the energy of the system for the initial configuration, the martensitic inclusion increases due to its eigenstrain ε^0 the global elastic energy $\int_V W\mathrm{d}V$ while the interface between the inclusion and the matrix increases the gradient energy density ψ^{grad}. Additionally, the points of the austenitic matrix (where $c = 0$) contribute to the separation potential. Initially, the global total energy $\int_V \psi\mathrm{d}V$ is minimized by decreasing the elastic energy. This could be done by degenerating the inclusion (Figure 6 (b)) which means reducing the eigenstrain ε^0 and thus, decreases the elastic energy. However, this mechanism increases the separation potential ψ^{sep} since the order parameter c is getting smaller in the area of the inclusion. Figure 3 shows that in a point, where the order parameter is decreasing starting from $c = 0.9$, the area of the global minimum is left, so that the separation potential ψ^{sep} increases. This can be seen in Figure 7, where the global separation energy $E^{\text{sep}} = \int_V = \psi^{\text{sep}}\mathrm{d}V$ is plotted as a function of simulation time. For the first few time steps the global separation energy E^{sep} is increasing strongly. Yet at a certain point, it becomes energetically more favorable for the system to decrease the separation energy E^{sep} instead of the elastic energy. So, in the area of the inclusion the order parameter c increases again to reach the global minimum of the separation potential ψ^{sep} at $c = 1$ (martensitic phase). Figure 6(c) shows the martensitic phase starting to grow in diagonal direction. This direction coincides with crystallographic (geometrical) theories (Wechsler et al. (1953)). The plate like shape of the martensitic phase, which can be observed in Figure 6(c) is in agreement with theoretical studies of the martensitic transformation, e. g. in Yamanaka et al. (2008).

When the martensitic plate has grown completely through the matrix, it expands its width until the matrix is completely martensitic (Figure 6(f)). For that configuration, all points of the system are in the global minimum of the separation potential ψ^{sep} at $c = 1$. Since for the global minimum $\psi^{\text{sep}} = 0$, the global separation energy $E^{\text{sep}} = 0$, too (see Figure 7).
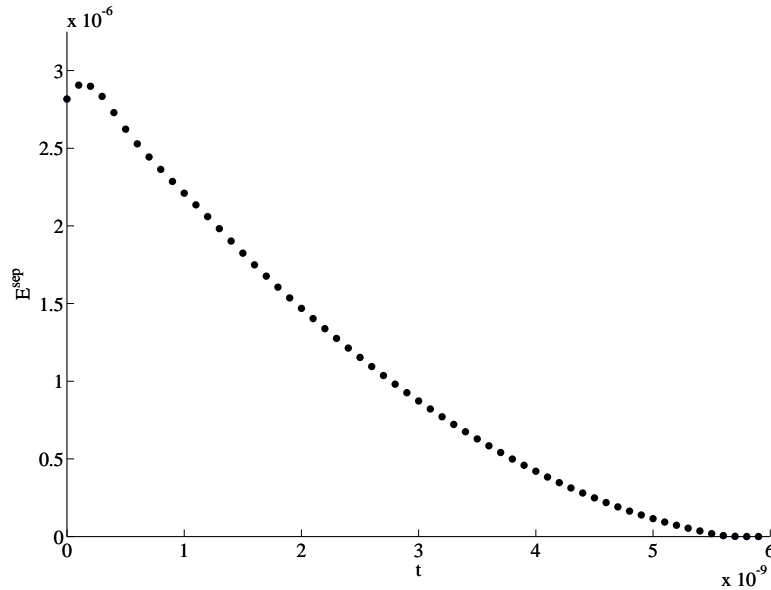
Figure 7: Global separation energy

6 Concluding Remarks

A phase field model for martensitic transformation is introduced. Initially, the model parameters are determined by comparison with MD simulation for pure iron for a temperature of 100 K. The parameters are verified for a temperature $T = 1300$ K, where the phase transformation in reverse direction led to the same result. By applying atomistic data for the continuum modeling we are able to study the martensitic transformation on a scale, which cannot be accessed by MD simulation.

Using the parameters gained in the first part for numerical simulations, an impact of external loads on the interface velocity could be detected, depending on the eigenstrain of the martensitic phase. Additionally, we studied the formation of the martensitic phase generated by a martensitic inclusion without external load applied. An accordance with theoretical studies and crystallographic theories could be shown. Furthermore, we focused on the energy evolution, which coincided with the growth of the martensitic phase.

7 Acknowledgements

References

Artemev, A.; Wang, Y.; Khachaturyan, A. G.: Three-dimensional phase field model and simulation of martensitic transformation in multilayer systems under applied stresses. *Acta Materialia*, 48, (2000), 2503–2518.

Bain, E. C.: The nature of martensite. *Transactions of the Metallurgical Society of AIME*, 70, (1924), 25–46.

Bartel, T.; Menzel, A.; Svendsen, B.: Thermodynamic and relaxation-based modelling of the interaction between martensitic phase transformations and plasticity. *Journal of Mechanics and Physics in Solids*, 59, (2011), 1004–1019.

Chen, L.-Q.; Wang, Y.; Khachaturyan, A. G.: Kintetics of tweed and twin formation during an ordering transition in a substitutional solid solution. *Philosophical Magazine Letters*, 65, (1992), 15–23.

Cherkaoui, M.; Berveiller, M.: Micromechanical modeling of the martensitic transformation induced plasticity in steels. *Smart Mater. Struct.*, 9, (2000), 592–603.

Daw, M. S.; Foiles, S. M.; Baskes, M.: The embedded-atom method: a review of theory and applications. *Mat. Sci. Rep*, 9, (1993), 251.

Engin, C.; Sandoval, L.; Urbassek, H. M.: Characterization of fe potentials with respect to the stability of the bcc and fcc phase. *Model. Simul. Mater. Sci. Eng.*, 16, (2008), 035005.

Entel, P.; Kreth, M.; Meyer, R.; Kadau, K.: Vibrational behavior of nanocrystalline materials. In: P. Vincenzini; F. Zerbetto, eds., *Modeling and simulating materials nanoworld*, vol. 44 of *Advances in Science and Technology*, page 2209, Techna Group (2004).

Entel, P.; Meyer, R.; Kadau, K.: Molecular dynamics simulations of martensitic transformations. *Philos. Mag. B*, 80, (2000), 183.

Entel, P.; Meyer, R.; Kadau, K.; Herper, H. C.; Hoffmann, E.: Martensitic transformations: First-principles calculations combined with molecular-dynamics simulations. *Eur. Phys. J. B*, 5, (1998), 379.

Fischer, F. D.; Berveiller, M.; Tanaka, K.; Oberaigner, E. R.: Continuum mechanical aspects of phase transformations in solids. *Archive of Applied Mechanics*, 64, (1994), 54–85.

Frenkel, D.; Smit, B.: *Understanding molecular simulation*. Academic, San Diego, 2nd edn. (2002).

Hildebrand, F. E.; Miehe, C.: Comparison of two bulk energy approaches for the phasefield modeling of two-variant martensitic laminate microstructure. *Technische Mechanik*, 32, (2011), 3–20.

Jin, Y. M.; Artemev, A.; Khachaturyan, A. G.: Three-dimensional phase field model of low-symmetry martensitic transformation in polycrystal: simulation of ζ_2'-martensite in aucd alloys. *Acta Materialia*, 49, (2001), 2309–2320.

Kadau, K.; Entel, P.: Atomistic study of the structural transformation in thin iron films on copper. *J. Magn. Magn. Mater.*, 198-199, (1999), 531.

Kadau, K.; Meyer, R.; Entel, P.: Molecular-dynamics study of thin iron films on copper. *Surf. Rev. Lett.*, 6, (1999), 35.

Kundin, A.; Raabe, D.; Emmerich, H.: A phase-field model for incoherent martensitic transformations including plastic accomodation process in the austenite. *Journal of Mechanics and Physics in Solids*, 59, (2011), 2082–2102.

Levitas, V. I.; Lee, D.-W.; Preston, D. L.: Interface propagation and microstructure evolution in phase field models of stress-induced martensitic phase transformations. *International Journal of Plasticity*, 26, (2009), 395–422.

Mei, J.; Davenport, J. W.: Free-energy calculations and the melting point of al. *Phys. Rev. B*, 46, (1992), 21.

Meyer, R.; Entel, P.: Martensite - austenite transition and phonon dispersion curves of $Fe_{1-x}Ni_x$ studied by molecular dynamics simulations. *Phys. Rev. B*, 57, (1998), 5140.

Miller, M. A.; Reinhardt, W. P.: Efficient free energy calculations by variationally optimized metric scaling: Concepts and applications to the volume dependence of cluster free energies and to solidsolid phase transitions. *J. Chem. Phys*, 113, (2000), 7035.

Nishiyama, Z.: X-ray investigation of the mechanism of the transformation from face-centred cubic lattice to body-centred cubic. *Sci. Rep. Tohoku Imp. Univ.*, 23, (1934), 637.

Pimpinelli, A.; Villain, J.: *Physics of Crystal Growth* (1998).

Sandia: http://lammps.sandia.gov/ (1997-2012).

Sandoval, L.; Urbassek, H. M.: Finite-size effects in fe-nanowire solid-solid phase transitions: a molecular dynamics approach. *Nano Lett*, 9, (2009a), 2290.

Sandoval, L.; Urbassek, H. M.: Solid-solid phase transitions in fe-nanowires induced by axial strain. *Nanotechnology*, 20, (2009b), 325704.

Sandoval, L.; Urbassek, H. M.: Transformation pathways in the solid-solid phase transitions of iron nanowires. *Appl. Phys. Lett*, 95, (2009c), 191090.

Sandoval, L.; Urbassek, H. M.; Entel, P.: The bain versus nishiyama-wassermann path in the martensitic transformation of fe. *New J. Phys*, 11, (2009a), 103027.

Sandoval, L.; Urbassek, H. M.; Entel, P.: Solid-solid phase transitions and phonon softening in an embedded-atom method model for iron. *Phys. Rev. B*, 80, (2009b), 214108.

Schmitt, R.; Mueller, R.; Kuhn, C.; Urbassek, H. M.: A phase field approach for multivariant martensitic transformations of stable and metastable phases. *Archive of Applied Mechanics*, DOI 10.1007/s00419-012-0721-6.

Schrade, D.; Mueller, R.; Xu, B.; Gross, D.: Domain evolution in ferroelectric materials: a continuum phase field model and finite element implementation. *Computer methods in applied mechanics and engineering*, 196, (2007), 4365–4374.

Schrade, D.; Xu, B. X.; Mueller, R.; Gross, D.: On phase field modeling of ferroelectrics: parameter identification and verification. *SMASIS*, 1, (2008), 299–306.

Urbassek, H. M.; Sandoval, L.: *Phase transformations in steels*, vol. 2: Diffusionless transformations, high strength steels, modelling and advanced analytical techniques. Woodhead Publishing Limited, Cambridge, UK (2012).

Wang, B.; Urbassek, H. M.: Phase transitions in an Fe system containing a bcc/fcc phase boundary: An atomistic study. *Phys. Rev. B*, 87, (2013), 104108.

Wang, Y.; Khachaturyan, A. G.: Three-dimensional field model and computer modeling of martensitic transformations. *Acta Materialia*, 2, (1997), 759–773.

Wassermann, G.: Einflüsse der α-γ-Umwandlung eines irreversiblen Nickelstahls auf Kristallorientierung und Zugfestigkeit. *Arch. Eisenhüttenwes.*, 6, (1933), 347.

Wechsler, M. S.; Lieberman, D. S.; Read, T. A.: On the theory of the formation of martensite. *Journal of Metals*, November, (1953), 1503–1515.

Yamanaka, A.; Takaki, T.; Tomita, Y.: Elastoplastic phase-field simulation of self- and plastic accommodations in cubic $\rightarrow$ tetragonal martensitic transformation. *Material Sience and Engineering A*, 491, (2008), 378–384.

Address: R. Schmitt, Institute of Applied Mechanics, University of Kaiserslautern, Gottlieb-Daimler-Straße, D-67663 Kaiserslautern,
R. Müller, dto.,
B. Wang, Physics Dept. and Research Center OPTIMAS, University of Kaiserslautern, Erwin-Schrödinger-Straße, D-67663 Kaiserslautern
H. M. Urbassek dto.
email: `rschmitt@rhrk.uni-kl.de`